Advances in Geo-Energy Research

Vol. 16, No. 2, p. 158-170, 2025

Original article

Permeability prediction in hydrate-bearing sediments via pore network modeling

Yongchao Zhang[1,2], Lele Liu[3]*, Liang Luo[4]*, Jingsheng Ma[5], Yunkai Ji[1,2], Ting Xiao[6], Nengyou Wu[2]

[1]*The Key Laboratory of Gas Hydrate, Ministry of Natural Resources, Qingdao Institute of Marine Geology, Qingdao 266237, P. R. China*

[2]*Laboratory for Marine Mineral Resources, Qingdao Marine Science and Technology Center, Qingdao 266237, P. R. China*

[3]*Shandong Engineering Research Center of Marine Exploration and Conservation, Ocean University of China, Qingdao 266100, P. R. China*

[4]*College of Physics and Electronics, Hunan Institute of Science and Technology, Yueyang 414000, P. R. China*

[5]*Institute of GeoEnergy Engineering, Heriot-Watt University, Edinburgh EH14 4AS, UK*

[6]*Energy & Geoscience Institute, The University of Utah, Salt Lake City 84108, US*

Keywords:
Natural gas hydrates
permeability prediction
pore network modeling
pore-structure characteristics

Cited as:
Zhang, Y., Liu, L., Luo, L., Ma, J., Ji, Y., Xiao, T., Wu, N. Permeability prediction in hydrate-bearing sediments via pore network modeling. Advances in Geo-Energy Research, 2025, 16(2): 158-170.
https://doi.org/10.46690/ager.2025.05.07

Abstract:
Natural gas hydrates in marine sediments undergo phase transitions under non-equilibrium conditions, making it challenging to accurately measure the permeability characteristics of hydrate-bearing sediments using experimental methods. In this study, pore network modeling is utilized to simulate the hydrate formation process and investigate the single-phase and two-phase permeability of hydrate-bearing sediments, and a comparative analysis was performed on consolidated and unconsolidated sediment samples. The results revealed the evolution of effective permeability as a function of hydrate saturation, and quantitative relationships were observed for the water retention curves and gas-water relative permeability, emphasizing the influence of pore structure and hydrate distribution on flow behavior. On the basis of the simulation results, predictive methods for irreducible water saturation, maximum water saturation, and key parameters in the van Genuchten and Brooks-Corey models for hydrate-bearing sediments are proposed. The findings provide deeper insights into gas-water flow dynamics in hydrate-bearing sediments and offer valuable guidance for hydrate resource exploitation, the assessment of environmental risks associated with hydrate dissociation, and the evaluation of carbon sequestration potential.

1. Introduction

Natural gas hydrates are compounds formed from gas and water under high-pressure, low-temperature conditions, predominantly found in marine and permafrost regions (Boswell et al., 2011; Wu et al., 2011). Due to their vast reserves and immense capacity to contribute to low carbon emissions, they are considered a promising potential energy resource (Boswell et al., 2020). Conservative estimates suggest that the total carbon content in natural gas hydrates is approximately twice that of all fossil fuels combined (Ruppel and Kessler, 2017). Therefore, the safe and efficient development of hydrates has been a major research focus over the past 30 years (Lu et al., 2023). However, beyond energy development, hydrates are also of interest in other fields, being studied as by-products in the pipelines of oil and gas transportation (Koh et al., 2002), as contributors to submarine disasters (Gong et al., 2022; Azimi et al., 2024) and global greenhouse effects (Yu et al., 2021), and as potential media for carbon dioxide sequestration (Zheng

Yandy Scientific Press

*Corresponding author.
E-mail address: yongchao.zhang@hotmail.com (Y. Zhang); lele.liu@ouc.edu.cn (L. Liu); fuboyi314@gmail.com (L. Luo); Jingsheng.Ma@hw.ac.uk (J. Ma); jiyunkai@yeah.net (Y. Ji); txiao@egi.utah.edu (T. Xiao); wuny@ms.giec.ac.cn (N. Wu).

Received March 13, 2025; revised April 5, 2025; accepted April 27, 2025; available online May 2, 2025.

et al., 2020).

Permeability governs the flow behaviors of fluids within porous media, influencing the processes relating to the rate of methane escape from sediments into seawater (Ruppel and Kessler, 2017), the locations of hydrate accumulation (You et al., 2019), the efficiency of CO_2 sequestration through hydrate technology (Zheng et al., 2020), and the gas production efficiency during hydrate exploitation (Cui et al., 2018; Li et al., 2021). Hydrate-Bearing Sediments (HBS) consist of four phases: Sediment particle, water, gas, and hydrate. At non-equilibrium states, the hydrate phase decomposes into water and gas, and therefore induces the permeability evolution of HBS in a more complicated manner than that in conventional oil and gas reservoirs (Li et al., 2024). The permeability of HBS under different hydrate saturations is described in terms of effective permeability for single-phase fluid flow and relative permeability for gas-water two-phase flow (Cai et al., 2020a; Xia et al., 2024). Experimental studies have extensively shown that the content and distribution of hydrates are critical factors controlling the permeability of HBS (Seol and Kneafsey, 2011; Zhao and Zhou, 2020). Solid-phase hydrates obstruct fluid flow in the pores, leading to reduced permeability, with the effective permeability of one fluid phase showing an approximately exponential relationship with hydrate saturation (He et al., 2023). Additional factors influencing the permeability of HBS include pore-structure factors such as pore radius, pore connectivity and porosity (Liu et al., 2020; Pan et al., 2021; Sun et al., 2021; Zhang et al., 2021; Xia et al., 2023). These factors not only restrict fluid flow but also impact the content and distribution of hydrates within the pores. However, the relationships between pore structures, hydrate content and distribution, and HBS permeability have not been accurately explained in the literature, largely due to experimental challenges in permeability measurements. These challenges include maintaining the phase equilibrium conditions of hydrates, preventing mass transfer and blockage of sediment particles, avoiding hydrate formation in unexpected locations, accurately determining hydrate content within the sediments, and minimizing permeability changes caused by pressure differences (Lei and Santamarina, 2018). Consequently, the permeability results of HBS reported in the literature exhibit multiple discrepancies. Besides, most reported studies focus on the effective permeability of single-phase flow, while fewer have addressed the relative permeability of gas-water phases flow in HBS.

Pore Network Modeling (PNM) has been widely adopted as an effective method for analyzing the permeability of HBS (Cai et al., 2020b). The working principle of PNM involves simplifying the pore spaces of porous media into a network of connected geometric elements, which can be subsequently used for property simulations (Ma et al., 2014). Many researchers (Wu et al., 2020; Luo et al., 2022) have applied PNM to pore networks extracted from Computed Tomography (CT) images of HBS samples taken at varying hydrate saturations, in order to assess the characteristics of permeability evolution and influencing factors. This approach ensures that the topological characteristics of the established pore networks closely align with those of the experimental HBS samples. However, there have been a limited number of completed CT experiments, which restricts the scope of these simulations, making it difficult to fully capture the evolution of pore-structure characteristics and permeability of HBSs under a wide range of conditions (Chen et al., 2018). An alternative approach, which has been widely adopted to achieve its purpose, is to simulate hydrate reaction processes within synthetic and extracted pore networks. Jang and Santamarina (2011) explored the flow properties by utilizing PNM within a randomly generated cubic network. In their study, hydrate dissociation is described by the change in hydrate content under varying temperature and pressure conditions and governed by the Peng-Robinson equation. Mahabadi et al. (2016a, 2019) utilized the maximal ball algorithm to extract pore networks from sediment CT images. On those pore networks, they randomly distributed hydrates in pores at variable situations to mimic the hydrate distribution patterns observed in experiments and derived the permeability curves and Water Retention Curves (WRCs) (Mahabadi et al., 2016b; Yan et al., 2020). Similarly, Dai and Seol (2014) applied a mathematical random approach to model hydrate formation in PNM simulations. They investigated the relationship between the effective permeability of HBS and the rate of hydrate formation, described by the number of pore elements occupied by hydrates at each computational step. Based on simulations, they proposed quantitative relationships linking permeability, hydrate saturation and key pore structure factors (e.g., porosity, hydraulic tortuosity) in HBS. In the study by Li et al. (2020), the formation of hydrate in the pore networks preferentially occurs in either the largest or the smallest pore. They analyzed the influences of pore size distribution and hydrate saturation on the WRCs and gas-water relative permeability. Nonetheless, the random distributions of hydrates as considered above do not take the physical foundations of hydrate formation into account, which can make hydrates occupy pore space incorrectly and in turn lead to unphysical hydrate configurations in pore space in pore networks. On such pore networks, flow simulation cannot reveal true relationships between the pore-structure characteristics and permeability properties for single-phase and multiphase fluids in HBS.

To address the aforementioned challenges, this study developed a PNM model on the basis of assumptions from the hydrate kinetics theory to model the hydrate formation and single-/two-phase flow processes in HBSs. To construct pore networks, CT scanning images of eight sedimentary samples of varying pore-structure characteristics, that is, four consolidated and four unconsolidated samples, were comparatively utilized. The simulation results generated from this approach included effective permeability, WRC, and gas-water relative permeability under different hydrate saturation conditions in HBSs.

2. Methodology and materials

2.1 Samples and CT images

To construct the pore network of HBSs, this study utilized grayscale CT images of four consolidated samples and four unconsolidated samples. All four consolidated samples (CS

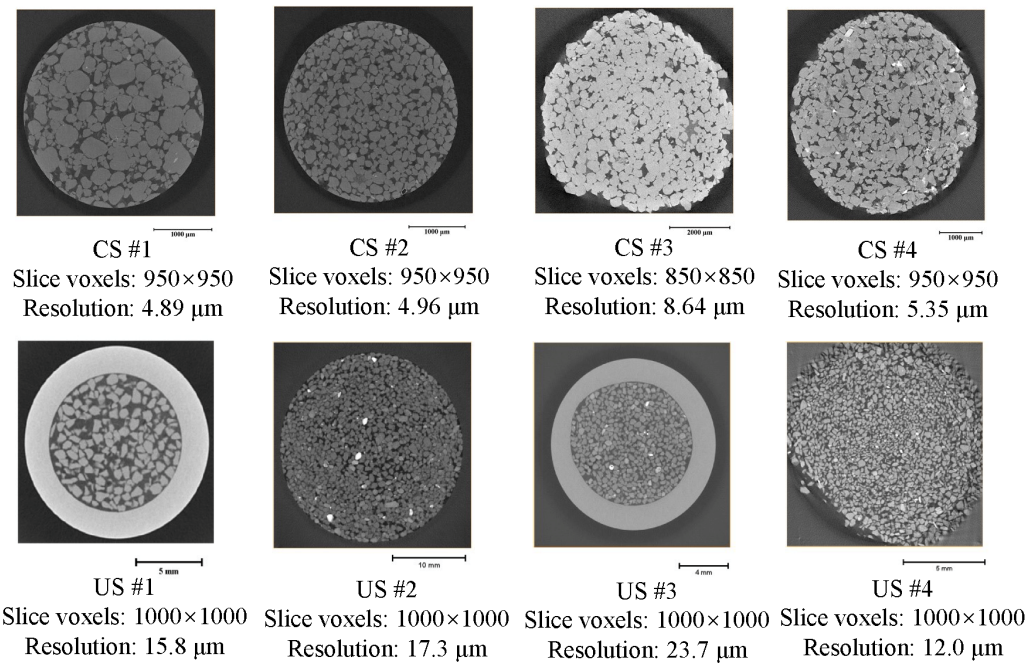

Fig. 1. 2D cross-section slices of CT images of the samples.

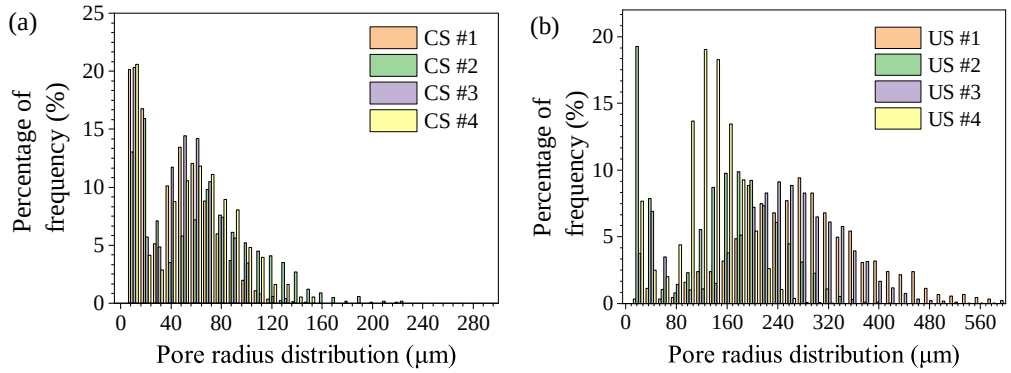

Fig. 2. Curves of pore radius distribution for the (a) consolidated and (b) unconsolidated samples.

#1, CS #2, CS #3, and CS #4) were sandstone specimens, and their CT images are open-source data available from Imperial College London (Blunt et al., 2013). The four unconsolidated samples (US #1, US #2, US #3, and US #4) were manmade in laboratories by compacting quartz-rich sand grains, and CT images for all samples were obtained using a Phoenix v|tome|x X-ray scanner from Qingdao Institute of Marine Geology. The selected Two-Dimensional (2D) slices for each CT image of the eight samples are shown in Fig. 1, and the pore size distribution for all samples are given in Fig. 2. The basic physical parameters of the eight samples, calculated from the CT images, are provided in Table 1. The extraction of pore network from images was performed using the Modified Maximum Ball Method (Dong and Blunt, 2009).

CS #1, CS #2, CS #3, and CS #4 were consolidated sandstone samples, while US #1, US #2, US #3, and US #4 were unconsolidated sediment samples composed of mixed quartz sand or sea sand. The CT source data of these samples are available from the authors upon request.

2.2 Assumptions of the PNM model

The PNM model can simulate the hydrate formation process and calculate gas-water flow in HBS samples. The development of this model is based on several assumptions derived from hydrate formation kinetics theories. For the applicability of these theories in modeling the hydrate formation process and the fundamental theoretical knowledge of formation kinetics, readers may refer to our previously published paper (Zhang et al., 2022a) and other relevant literature (Dai and Seol, 2014; Kvamme, 2021). The main assumptions of this model are given as follows:

1) The hydrate formation process can be divided into a hydrate nucleation stage and a subsequent hydrate growth stage (Kvamme, 2021; Zhang et al., 2022b).
2) Hydrate nucleation sites are randomly distributed within the pores (Sloan Jr and Koh, 2007). A coefficient, referred to as the nucleation fraction (F_n), controls the number of hydrate nucleation sites, representing the ratio of pores

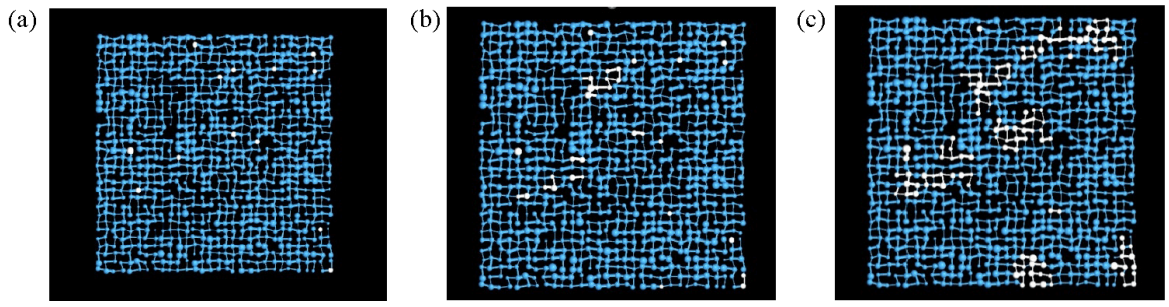

Fig. 3. Schematic showing the simulation of hydrate nucleation and growth process in the two-dimensional model. (a) Distribution of hydrates after the nucleation process, (b) the initial growth process of hydrates and (c) the progressive growth process of hydrates. In the figures, spherical and cylindrical elements represent pores and throats, respectively. Blue indicates the elements occupied by the water phase, and white indicates those occupied by the hydrate phase.

Table 1. Pore-scale properties of the samples obtained from CT images.

Sample	Permeability (D)	Porosity (%)	Pore coordination (-)	Pore tortuosity (-)	Mean grain radius (μm)
CS #1	7.897	25.1	2.38	2.21	60.3
CS #2	1.154	24.6	2.53	1.87	60.3
CS #3	1.483	14.1	1.75	2.32	113.1
CS #4	1.107	19.5	2.08	1.84	58.8
US #1	27.268	42.1	4.57	1.34	420.2
US #2	124.368	34.2	3.99	1.38	347.0
US #3	77.459	34.3	4.18	1.66	236.3
US #4	61.470	45.4	4.86	1.36	121.1

with nucleation to the total number of pores.

3) Hydrate growth occurs after the nucleation stage, driven by the water activity within pore elements. Hydrates preferentially form in pores with higher water activity (Azimi et al., 2021).
4) The hydrate growth among pores is also influenced by interfacial interactions, with hydrates preferentially forming in pores near the contact interface between the hydrate phase and the water phase.
5) Hydrates entirely fill the pores once they nucleate or form in the pores or throats (Mahabadi et al., 2016a), which reflects the influence of the Ostwald ripening effect (Xu and Yoshihiro, 2025).
6) The effects of gas-water interfaces, clay swelling and hydration on hydrate reactions and fluid flow are ignored.

Two concepts regarding the above model assumptions need to be explained. Firstly, water activity is defined as a measure of water that is available to react with another material (Clarke et al., 1999). In porous media, the activity of pore water (a_w) can be characterized as a function of pore radius (r), contact angle of the mineral surface (θ), surrounding temperature (T), interfacial tension between mineral and water (σ), and the volume of water in the pore (V), as shown in Eq. (1). Applications of using water activity in predicting the hydrate formation in porous media have proved feasible in some thermodynamic works (Chen et al., 2010; Azimi et al., 2021). In our developed model, water activity is used to control the sequence of hydrate growth at the hydrate-fluid interface:

$$a_w = \mathrm{e}^{-2\sigma V\cos\theta/(rRT)} \tag{1}$$

Another parameter that requires explanation is the nucleation fraction defined in the model. In natural sediments, the hydrate nucleation process is influenced by various factors such as temperature, pressure, impurities, pore water salinity, nanobubbles, microorganisms, and clay mineral particles (Sloan Jr and Koh, 2007; Zhang et al., 2022b). It is generally believed that the location and timing of hydrate nucleation are rather stochastic, making the prediction of this process difficult. In our model, the nucleation fraction is utilized to control the proportion of pores where hydrate nucleation occurs. However, this parameter must be validated against experimental measurements.

Fig. 3 illustrates the simulation processes of hydrate nucleation and growth showing in the two-dimensional model. In the hydrate nucleation process, the positions of nucleation are determined by using a stochastic function, with the total number of nucleation pores constrained by the nucleation fraction parameter (Fig. 3(a)). Initial hydrate growth preferentially occurs in pore elements adjacent to nucleation sites, which are selected based on comparing the water activity levels of the surrounding pore elements (Fig. 3(b)). During subsequent growth stages, water-phase pores surrounding hydrate-phase

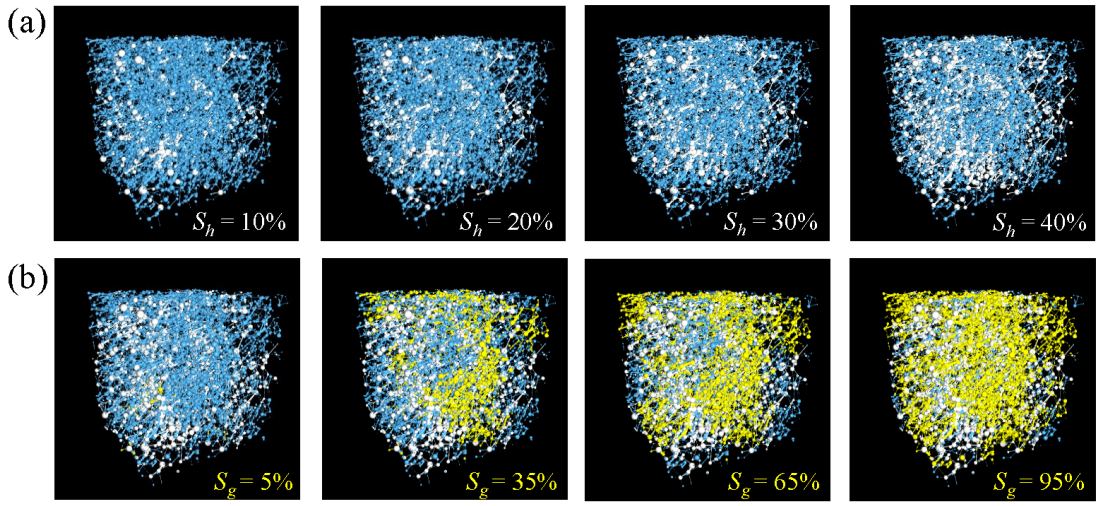

Fig. 4. Simulation workflow of hydrate formation and gas-water flow in sediment samples using the constructed PNM (illustrated with CS #4 as an example): (a) Hydrate formation process and (b) gas invasion process. In the figure, the yellow elements indicate those occupied by the gas phase, and the representation of other elements is consistent with that in Fig. 3.

pores gradually convert to hydrate-phase pores, leading to increasing hydrate saturation and decreasing water saturation (Fig. 3(c)).

2.3 Workflow of PNM simulations

The workflow for simulating hydrate formation and calculating gas-water flow using the constructed PNM is presented below, with Fig. 4 illustrating the procedural steps.

- Step 1: Initiate all the pores and throats of the network to be fully saturated with water.
- Step 2: Simulate the hydrate nucleation process using a set nucleation fraction, followed by the hydrate growth process. During this stage, hydrate saturation gradually increases in the sample (Fig. 4(a)).
- Step 3: Pause the hydrate growth once hydrate saturation reaches the first predefined threshold.
- Step 4: Initiate gas invasion from the bottom inlet to displace water in the pores and throats, with gas saturation increasing from 0 (Fig. 4(b)).
- Step 5: After gas completely invades all water-filled pores in the network, reset the model to its state before gas invasion and resume the hydrate growth process starting from the first predefined hydrate saturation threshold.
- Step 6: Repeat the cycle of hydrate growth and gas invasion, pausing at subsequent predefined thresholds of hydrate saturation.
- Step 7: Complete the iterative process to obtain gas-water relative permeability and other parameters under varying hydrate saturations.

The processes of hydrate formation and gas-water displacement in the networks are realized by employing the quasi-static method, and the permeability properties are calculated based on the conductivity correlations between the pores and throats. These solution methods and calculation approaches are well-established in petroleum research, and readers can find detailed descriptions in the cited references (Blunt et al., 2013; Boujelben, 2017). It should be emphasized that while wettability effects are incorporated into the calculation of water activity and capillary pressure, the model does not account for the corner flow and layer flow mechanisms induced by wettability (Yang et al., 2021). Additionally, the hydrate phase as a solid is assumed not to participate in the gas-water flow. The relative permeability of the gas and water phases in the results is determined by calculating the effective permeability of each phase as a fraction of the absolute permeability in the absence of hydrate.

In this study, the user interface and solver of the computations of the developed model could be implemented based on an open-source PNM code numSCAL (Boujelben, 2017), for which the authors would like to express their gratitude.

2.4 Validation of model prediction

Accurately determining the nucleation fraction is critical for reliable predictions of the permeability of HBS. However, the number of hydrate nucleation sites cannot be obtained through measurement using the current technology. In this case, the validation strategy employed in this study aims to fit the effective permeability-hydrate saturation relationship controlled by the nucleation fraction and then inversely determine the reasonable value of nucleation fraction setting in the PNM model. To validate the accuracy of model prediction, the pore network of Berea sandstone (corresponding to CS #4 in this study) was selected to perform 100 simulations with nucleation fraction values ranging from 0.001 to 0.1, and the simulation results were compared with the experimental effective permeability of Berea sandstones from published studies (Yousif et al., 1991; Kleinberg et al., 2003; Sourav and Angus, 2021). All these experimental results were obtained from hydrate formation experiments using Berea samples. Fig. 5 shows that when the nucleation fraction is set to 0.02, the simulation results agree well with the experimental data. It should be emphasized again that this nucleation fraction is d-

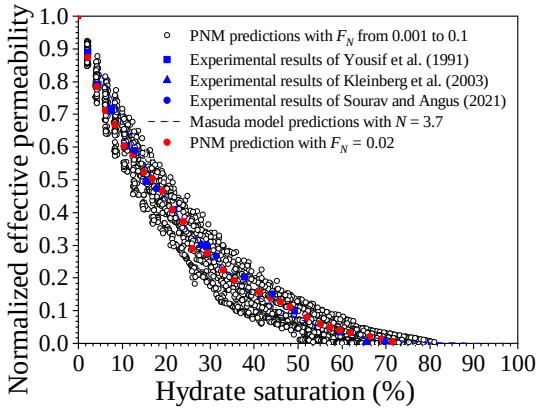

Fig. 5. Comparison of PNM predictions and experimental measurements of effective permeability under different nucleation fractions.

erived through regression from experimental data, while actual measurements may differ from model predictions due to potential variations in the experimental conditions.

3. Results and discussion

3.1 Effective permeability

Fig. 6 shows the variation in effective permeability with hydrate saturation in different samples as calculated by the PNM. The results for consolidated and unconsolidated samples are presented separately in Figs. 6(a) and 6(b), respectively. It can be seen that, as hydrate saturation increases, the effective permeability of all samples follows an exponential decline. However, unconsolidated samples in Fig. 6(b) exhibit smoother curves, while consolidated samples in Fig. 6(a) show some fluctuations. At lower hydrate saturations, the inhibitory effect of hydrates on fluid flow is more pronounced, resulting in a steeper decline in permeability. For example, with a 20% increase in hydrate saturation, the effective permeability of CS #1, CS #2, CS #3, and CS #4 decreases by 62.5%, 73.5%, 66.8%, and 64.4%, respectively. At higher hydrate saturations ($\geq$ 30%), the rate of permeability declines slows gradually. As hydrate saturation continues to increase beyond a certain threshold, the effective permeability of the sample eventually drops to zero, and this threshold is less than 100%. This indicates that even if hydrate does not completely fill all pores, the sample can become impermeable once localized flow paths are blocked. This phenomenon has been documented in previous studies (Chen et al., 2018; Mahabadi et al., 2019). In this study, this threshold is defined as the critical hydrate saturation (S_{ch}), which represents the minimum hydrate saturation at which the sample becomes impermeable. In comparison, the S_{ch} for consolidated samples is approximately 70%, while for unconsolidated samples, it is around 80% (Fig. 6 and Table 2). To analyze the controlling factors of Sch, a parameter characterizing the pore structure of the sediment is introduced, which incorporates porosity (ϕ), coordination number (C), and tortuosity (τ), as given in:

$$\alpha = \frac{C\sqrt[3]{\phi}}{\tau^2} \tag{2}$$

The numerator of this parameter is positively correlated with the permeability of the sample, while this correlation is negative for the denominator. After fitting, the relationship between the pore structure parameter and S_{ch} is expressed by (Fig. 7):

$$S_{ch} = \frac{0.1C\sqrt[3]{\phi}}{\tau^2} + 0.66 \tag{3}$$

The Tokyo model is the most commonly used model for predicting the effective permeability of HBS, which demonstrates the relationship between normalized effective permeability (K_{ne}) and hydrate saturation (S_h). It is an empirical function, expressed as $K_{ne} = (1 - S_h)^N$, where N is the permeability reduction coefficient. However, from the functional form of the Tokyo model, it assumes that the HBS remains permeable until hydrate saturation reaches 100%, without considering the existence of S_{ch}. Therefore, the predicted result from the Tokyo model may cause some errors at certain high hydrate saturation conditions. To address this issue, this study has modified the Tokyo model to incorporate the effect of S_{ch}, resulting in the modified Tokyo model, expressed by:

$$K_{ne} = \left(1 - \frac{S_h}{\frac{0.1C\sqrt[3]{\phi}}{\tau^2} + 0.66}\right)^{N'} \tag{4}$$

where N' represents the modified permeability reduction index. The permeability reduction coefficients and the modified coefficients for the samples, fitted using the two models, are listed in Table 2. Under the given coefficients, the standard squared deviations between the theoretical predictions of both models and the PNM results are larger than 0.98, indicating the good applicability of these models in predicting the effective permeability in HBSs. However, at high hydrate saturation levels, the modified Tokyo model may provide better predictive accuracy.

3.2 WRC

WRC describes the relationship between water saturation and capillary pressure in porous media, which is commonly used to study the water retention capacity and permeability characteristics of sediments (Yan et al., 2020). Fig. 8 shows the WRCs of HBS samples during the gas invasion process under different hydrate saturation conditions (0%, 10%, 20%, 30%, and 40%). It can be seen that, as hydrate saturation increases, the WRCs shift towards higher values on the Y-axis, indicating that higher capillary pressure is required to achieve the same water saturation during the two-phase flow process. Compared to the unconsolidated samples, the WRCs of the consolidated samples show a more significant shift as hydrate saturation changes. Additionally, the Y-axis values of the WRC for consolidated samples are significantly higher compared to unconsolidated samples, which is caused by the pore radius of consolidated samples being smaller than that of unconsolidated ones. Moreover, for each sample, both the gas entry pressure (the Y-coordinate at the far-right endpoint of the curve) and the irreducible water saturation (the X-coordinate at the far-left endpoint of the curve) gradually increase with rising hydrate

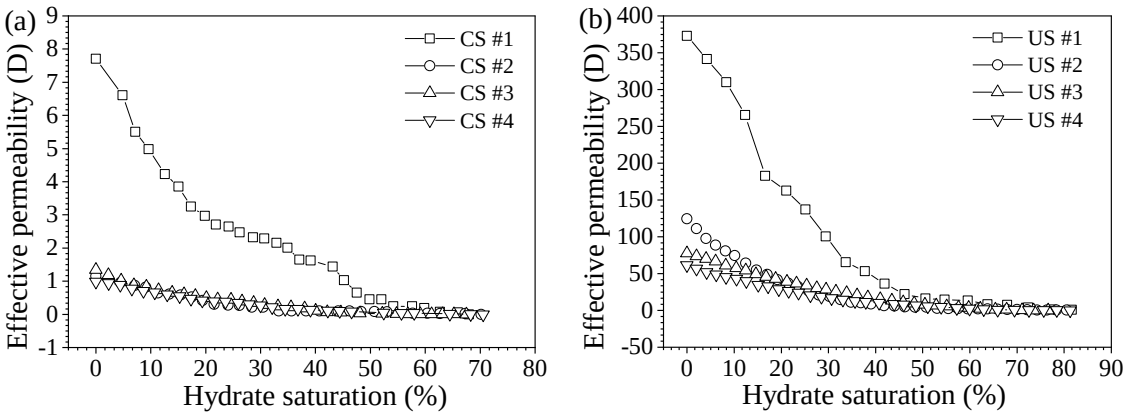

Fig. 6. Calculated effective permeability under different hydrate saturations in the (a) consolidated and (b) unconsolidated samples.

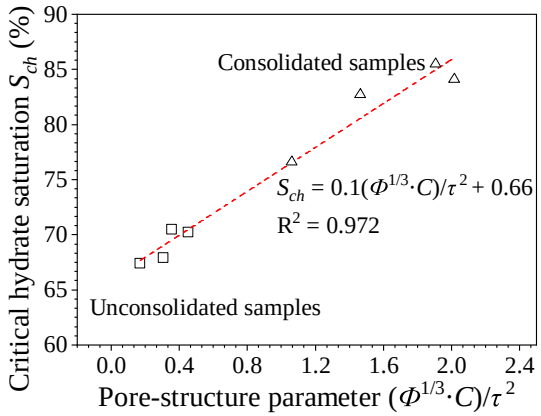

Fig. 7. Correlation between S_{ch} and pore-structure parameter in HBSs.

Table 2. Parameters related to effective permeability and fitting parameters with theoretical models in HBSs.

Sample	$C\sqrt[3]{\phi}/\tau^2$	S_{ch}	N	N'
CS #1	0.307	0.679	3.6	2.2
CS #2	0.454	0.702	4.4	2.8
CS #3	0.170	0.674	5.1	3.2
CS #4	0.356	0.705	4.4	2.7
US #1	1.906	0.855	3.8	3.2
US #2	1.464	0.827	5.3	4.0
US #3	1.063	0.766	3.0	2.1
US #4	2.018	0.841	3.5	2.8

saturation. The irreducible water saturation is generally higher in consolidated samples compared to unconsolidated ones.

On the basis of the obtained WRC results, the Van Genuchten (VG) model for WRC predictions (shown as Eq. (5)) were used to evaluate the water retention characteristics of different HBS samples:

$$P_c = P_{ge}\left[\left(\frac{S_w - S_{rw}}{1 - S_{rw}}\right)^{-1/m} - 1\right]^{1-m} \tag{5}$$

where P_{ge} represents the gas entry pressure, S_w represents the water saturation, S_{rw} represents the irreducible water saturation, and m is a fitting parameter. Fig. 9 presents the variation of the fitted parameters m and gas entry pressure across different samples as a function of hydrate saturation. As shown in the figure, both m and gas entry pressure exhibit linear correlations with hydrate saturation. Specifically, the parameter m decreases linearly with increasing hydrate saturation, while the gas entry pressure increases linearly with it. For the four samples of the same type, the slopes of the evolution curves of the fitting parameter m and gas entry pressure with respect to hydrate saturation are similar; however, the intercepts of these curves on the axis differ. The slope of$m$ variation with hydrate saturation is smaller for consolidated samples than that for unconsolidated samples. The fitted m values for these two types of samples are mainly within the range of $0.80 \sim 0.85$. In contrast, the slope and the fitted values of the gas entry pressure variation with hydrate saturation is notably larger for consolidated samples compared to unconsolidated samples. The gas entry pressure values for consolidated samples range from 0.8 to 1.4 MPa, whereas for unconsolidated samples, they range from 0.1 to 0.4 MPa. From the above results, the fitting parameter m and gas entry pressure in the VG model can be roughly predicted by:

$$\begin{aligned} m &= m_0 - 0.106S_h \\ P_{ge} &= P_{ge-0} + 0.6S_h \end{aligned} \tag{6}$$

For unconsolidated samples, these two parameters can be predicted by:

$$\begin{aligned} m &= m_0 - 0.043S_h \\ P_{ge} &= P_{ge-0} + 0.1S_h \end{aligned} \tag{7}$$

where m_0 and P_{ge-0} respectively denote the fitting parameter m and gas entry pressure of the sample under the hydrate-free condition.

3.3 Relative permeabilities

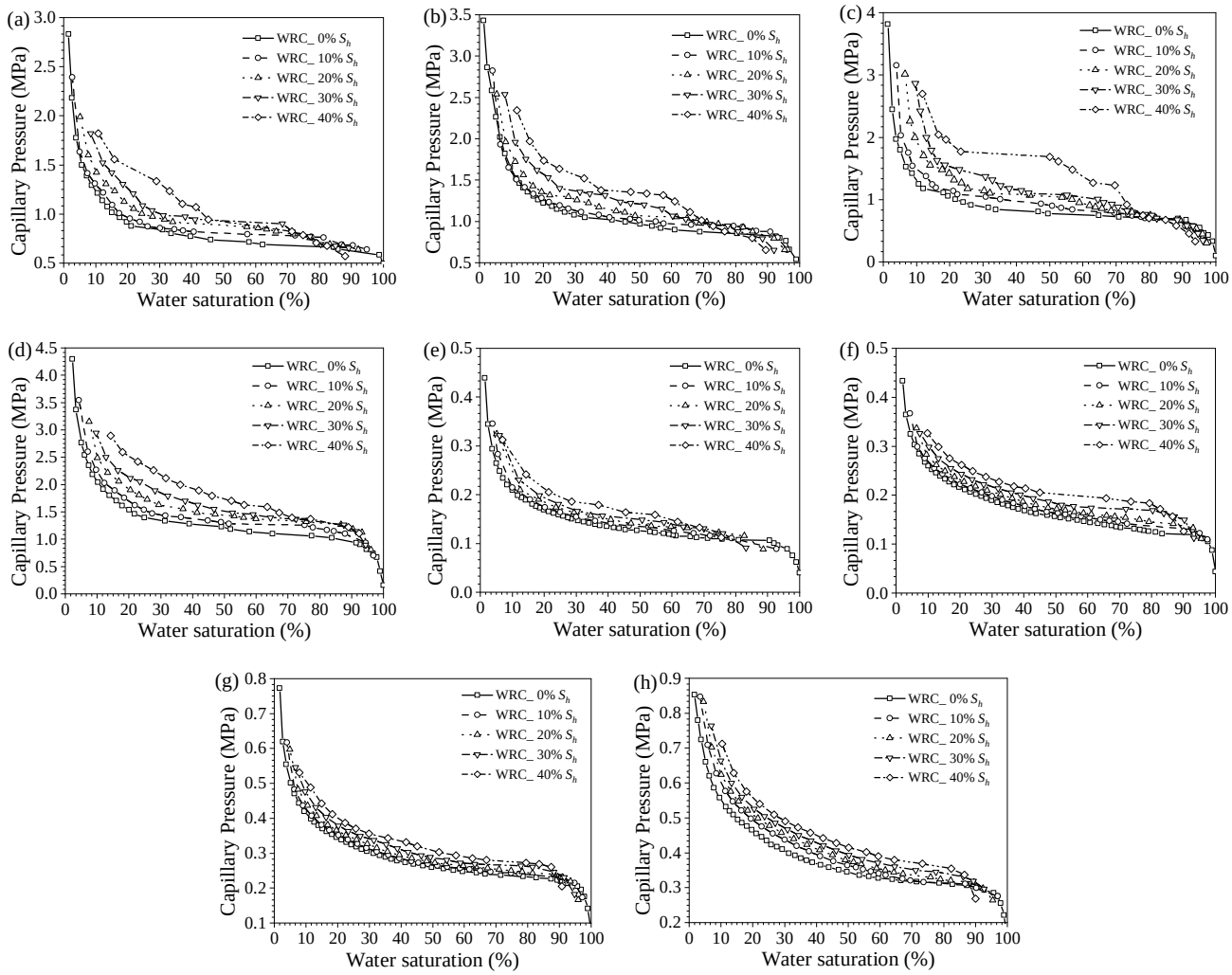

Fig. 8. WRCs of HBS samples at different hydrate saturations, (a)-(d) represent the WRC results of CS #1, CS #2, CS #3, and CS #4, (e)-(h) represent the WRC results of US #1, US #2, US #3, and US #4, respectively.

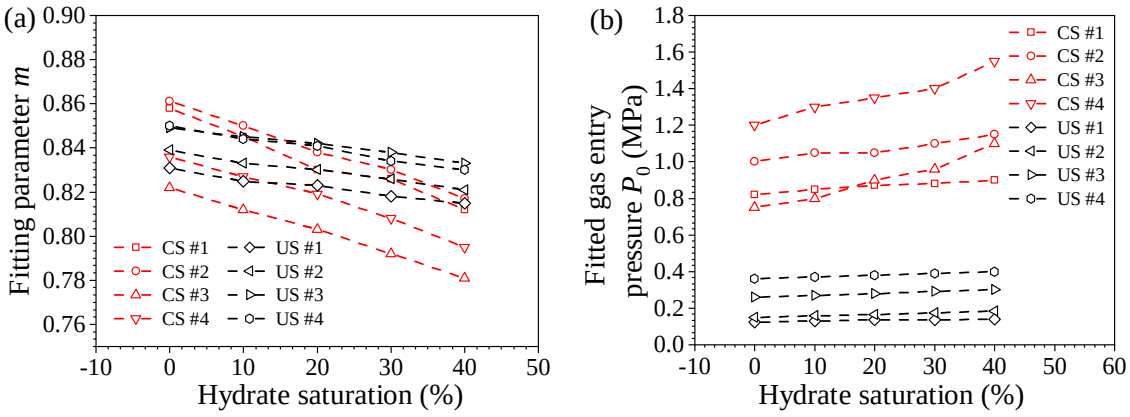

Fig. 9. Variation in the parameters m and gas entry pressure as a function of hydrate saturation obtained by fitting the WRC using the VG model. (a) Consolidated samples and (b) unconsolidated samples.

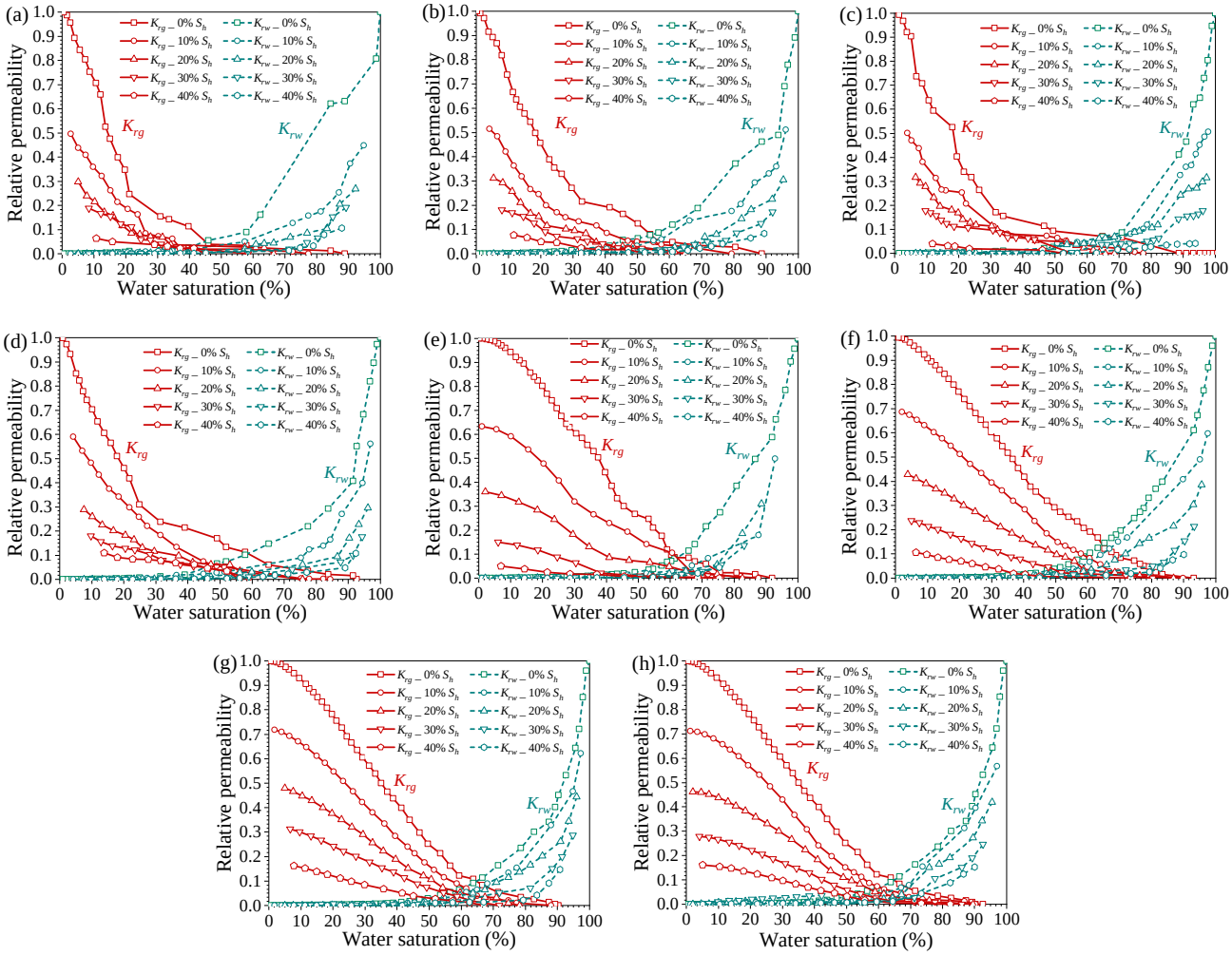

Fig. 10. Gas-water relative permeability curves of consolidated and unconsolidated samples under different hydrate saturations obtained from the developed PNM; (a)-(d) represent the results for CS #1, CS #2, CS #3, and CS #4, and (e)-(h) represent the results for US #1, US #2, US #3, and US #4, respectively.

3.3.1 Changes in relative permeability curves

Fig. 10 presents the gas-water relative permeability curves for both consolidated and unconsolidated samples at different hydrate saturations (0%, 10%, 20%, 30%, and 40%). It can be observed that the impact of hydrate content on the relative permeability varies among the sample types. For example, under 10% hydrate saturation, the gas-phase permeability in CS #1 decreases by 50% compared to the hydrate-free condition, while the decrease is about 37% in US #1. In addition to hydrate saturation, the relative permeability of HBS is also influenced by the pore structure of sediments. Consolidated samples, characterized by poorer pore connectivity, show a greater reduction in gas-water relative permeability. The shape of the relative permeability curves also differs between sample types. In unconsolidated samples, the gas-phase relative permeability curve exhibits a convex shape as water saturation changes, with a generally smoother curve. In contrast, the water-phase relative permeability curves in unconsolidated samples, as well as both gas-phase and water-phase curves in consolidated samples, exhibit a concave shape. This difference is primarily due to the better pore connectivity in unconsolidated samples, as well as the higher flow viscosity of the gas phase. As for at the endpoints of the relative permeability curves, the left endpoint on the X-axis, representing the irreducible water saturation (S_{rw}), increases as hydrate saturation rises. Meanwhile, the right endpoint, representing the maximum water saturation (S_{w_max}), decreases with increasing hydrate saturation. These changes in S_{rw} and S_{w_max} indicate that the two-phase flow region in HBSs shrinks gradually as the hydrate saturation increases. Furthermore, it can be observed that the intersection of the gas-phase and water-phase relative permeability curves, known as the equal permeability point, shifts slightly towards the left on the water saturation axis as hydrate saturation increases. Thus, it can be inferred that the presence of hydrates has a slightly greater impact on gas-phase relative permeability than that on water-phase permeability in HBS.

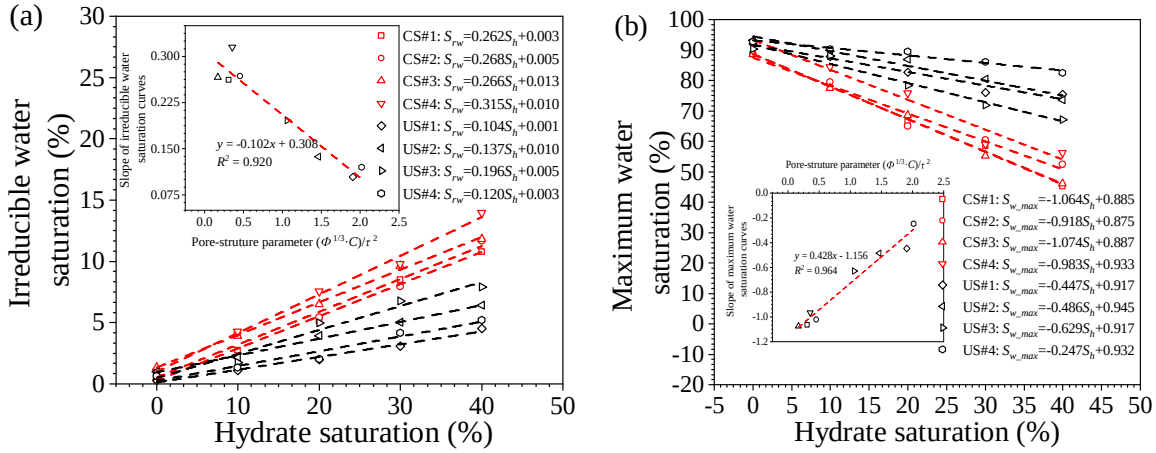

Fig. 11. Variation in S_{rw} and S_{w_max} with hydrate saturation in consolidated and unconsolidated samples. (a) Correlation between S_{rw} and S_h and (b) correlation between S_{w_max} and S_h.

3.3.2 Irreducible water saturation (S_{rw}) and maximum water saturation (S_{w_max})

Fig. 11 illustrates the variation in S_{rw} and S_{w_max} with hydrate saturation for both consolidated and unconsolidated samples. The results show a linear correlation between S_{rw} and S_{w_max} with hydrate saturation for both types of samples. As hydrate saturation increases, S_{rw} also increases while S_{w_max} decreases. The S_{rw} in the consolidated sample is higher compared to the unconsolidated sample, while the S_{w_max} is lower. At low hydrate saturations, the differences in S_{rw} and S_{w_max} between the two sample types are minimal; however, as hydrate saturation increases, the differences become more pronounced. In the subplots of Fig. 11, the slopes of the linear fits for S_{rw} and S_{w_max} are plotted against the pore-structure parameter α. The results indicate a good linear correlation between the slopes of S_{rw} and S_{w_max} curves with the parameter α. The intercepts of the fitting lines are similar across different samples, but the slope of the S_{rw} fitting line decreases linearly with the increase in α, while the slope of the S_{w_max} fitting line increases linearly. Based on these relationships, regression formulas can be derived for predicting S_{rw} and S_{w_max} in HBS for both consolidated and unconsolidated samples, as shown in:

$$S_{rw} = -\frac{0.1 S_h C \sqrt[3]{\phi}}{\tau^2} + 0.3 S_h + 0.01 \tag{8}$$

$$S_{w\_max} = \frac{0.4 S_h C \sqrt[3]{\phi}}{\tau^2} - 1.2 S_h + 0.9 \tag{9}$$

3.3.3 Fitting parameter values for the VG model and Brooks-Corey (BC) model

The formulas for the VG model and the BC model are expressed as shown in Eqs. (10)-(13). On the basis of the obtained S_{rw} and S_{w_max} results, the fitting parameters for different samples under varying hydrate saturations are further analyzed, including m_w and m_g in the VG model, and nw and ng in the BC model. The evolution of these four parameters with the hydrate saturation changing in consolidated and unconsolidated samples are plotted in Fig. 12.

$$K_{rw} = \sqrt{\frac{S_w - S_{rw}}{1 - S_{rw}}} \left\{ 1 - \left[1 - \left(\frac{S_w - S_{rw}}{1 - S_{rw}} \right)^{1/m_w} \right]^{m_w} \right\}^2 \tag{10}$$

$$K_{rg} = \sqrt{1 - \frac{S_w - S_{rw}}{S_{w\_max} - S_{rw}}} \left[1 - \left(\frac{S_w - S_{rw}}{S_{w\_max} - S_{rw}} \right)^{1/m_g} \right]^{2m_g} \tag{11}$$

$$K_{rw} = \left(\frac{S_w - S_{rw}}{1 - S_{rw}} \right)^{n_w} \tag{12}$$

$$K_{rg} = \left(\frac{S_g + S_{w\_max} - 1}{S_{w\_max}} \right)^{n_g} \tag{13}$$

where m_w represents the fitting parameter for water phase in the VG model, m_g represents the fitting parameter for the gas phase in the VG model, n_w represents the fitting parameter for the water phase in the BC model, and n_g represents the fitting parameter for the gas phase in the BC model.

From Fig. 12, it is evident that the four fitting parameters show good linear correlations with hydrate saturation across different samples. For consolidated samples (red markers in Fig. 12), all four fitting parameters exhibit linear decreases with increasing hydrate saturation, although the slopes of these linear relationships differ. The decreasing rate of these fitting parameters of consolidated samples is larger than that of unconsolidated ones. In addition, in unconsolidated samples (the black markers in Fig. 12), m_w in the VG model and n_w in the BC model decrease linearly with increasing hydrate saturation. However, m_g in the VG model and n_g in the BC model maintain a nearly constant value as hydrate saturation increases. The differences in the evolution of fitting parameters across different samples highlight the impact of pore structure on permeability. The complex pore structure and poor pore connectivity in consolidated samples lead to a more significant influence of hydrate saturation on gas-water relative permeability, resulting in a faster decline in the fitting parameters compared to the unconsolidated samples. In contrast, the better pore connectivity and higher mobility of gas phase in unconsolidated samples may contribute to

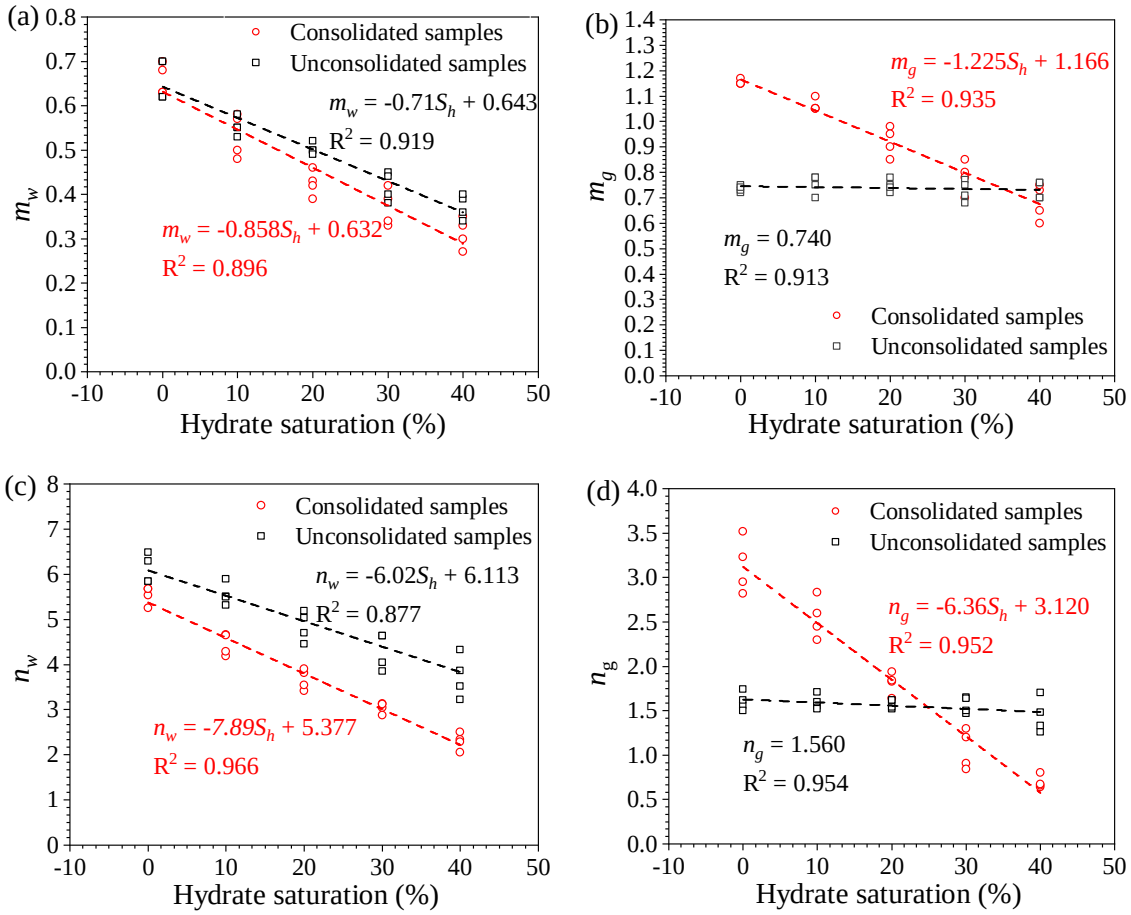

Fig. 12. Relationship between the fitting parameters and hydrate saturation in consolidated and unconsolidated samples. (a) m_w in VG model vs. S_h, (b) m_g in VG model vs. S_h, (c) n_w in BC model vs. S_h and (d) n_g in BC model vs. S_h.

Table 3. The recommended fitting parameters for relative permeability predictions.

Samples	VG model	BC model
Consolidated	$m_w = -0.858S_h + 0.632$, $m_g = -1.225S_h + 1.166$	$n_w = -7.893S_h + 5.377$, $n_g = -6.358S_h + 3.120$
Unconsolidated	$m_w = -0.710S_h + 0.643$, $m_g = 0.740$	$n_w = -6.022S_h + 6.113$, $n_g = 1.560$

the minimal variation in m_g and n_g with increasing hydrate saturation, as shown in Figs. 12(b) and 12(d), respectively. Based on the simulation and fitting results, the prediction expressions for the key parameters in the VG model and BC model are given in Table 3.

4. Conclusions

In this paper, a PNM simulation model incorporating assumptions derived from hydrate kinetics theory was utilized for analyzing the permeability characteristics of HBSs. Then, comparative analyses of the relationships were conducted between varying hydrate saturation and single-phase/two-phase permeabilities in consolidated and unconsolidated samples, leading to the following conclusions:

1) A critical hydrate saturation threshold (Sch) was identified, beyond which the permeability of HBS becomes effectively non-conductive. This threshold, which varies between consolidated and unconsolidated samples, is influenced by the pore structure parameters, including porosity, coordination number and tortuosity. The Sch values for consolidated samples were lower than those for unconsolidated samples.
2) The formation of hydrates in sediments affects the WRCs and relative permeability in HBSs. Increasing hydrate saturation results in higher capillary pressure at the same water saturation in WRC, lower gas and water relative permeability, and reduced two-phase flow region in relative permeability curves. Consolidated samples are more severely affected by hydrates in terms of both gas and water flow reduction.
3) Irreducible water saturation and maximum water saturation in HBSs show increasing and decreasing linear relationships, respectively, with increasing hydrate saturation.

The two parameters can be predicted based on the pore-structure characteristics of sediment.

4) The fitting parameters for the VG and BC models show strong linear correlations with hydrate saturation. The derived quantitative relationships between these parameters and hydrate saturation provide a reliable framework for predicting two-phase flow behaviors in HBS, offering a practical tool to better understand the interplay between hydrate saturation, pore structure and permeability.

The above findings provide critical insights into the permeability evolution in HBS, contributing to improved modeling for hydrate resource exploitation, as well as enhanced environmental risk assessments related to hydrate dissociation. This work also lays the foundation for future research on hydrate-based carbon sequestration and its potential environmental impact.

Acknowledgements

This work was supported by the Joint Geological Foundation of NSFC (No. U2444215), the National Key Research and Development Plan of China (No. 2023YFC2811001), the Natural Science Foundation of Shandong Province (No. ZR2022YQ54), and the Taishan Scholar Program (No. tsqn202306297). Jingsheng Ma acknowledges the NERC grant number NE/R018022/1 for financial support.

Conflict of interest

The authors declare no competing interest.

References

Azimi, A., Ansarpour, M., Mofarahi, M. Natural gas hydrate-related disasters and case studies, in Advances in Natural Gas: Formation, Processing, and Applications, edited by Mohammad Reza Rahimpour, Elsevier, pp. 191-207, 2024.

Azimi, A., Javanmardi, J., Mohammadi, A. H. Development of thermodynamic frameworks for modeling of clathrate hydrates stability conditions in porous media. Journal of Molecular Liquids, 2021, 329: 115463.

Blunt, M. J., Bijeljic, B., Dong, H., et al. Pore-scale imaging and modeling. Advances in Water Resources, 2013, 51: 197-216.

Boswell, R., Collett, T. S. Current perspectives on gas hydrate resources. Energy & Environmental Science, 2011, 4(4): 1206-1215.

Boswell, R., Hancock, S., Yamamoto, K., et al. Natural gas hydrates: Status of potential as an energy resource, in Future Energy, edited by Trevor M. Letcher, Elsevier, pp. 111-131, 2020.

Boujelben, A. H. A new pore-scale numerical simulator for investigating special core analysis data. Edinburgh, Heriot-Watt University, 2017.

Cai, J., Xia, Y., Lu, C., et al. Creeping microstructure and fractal permeability model of natural gas hydrate reservoir. Marine and Petroleum Geology, 2020a, 115: 104282.

Cai, J., Xia, Y., Xu, S., et al. Advances in multiphase seepage characteristics of natural gas hydrate sediments. Chinese Journal of Theoretical and Applied Mechanics, 2020b, 52(1): 208-223. (in Chinese)

Chen, L., Sun, C., Chen, G., et al. Thermodynamics model of predicting gas hydrate in porous media based on reaction-adsorption two-step formation mechanism. Industrial & Engineering Chemistry Research, 2010, 49(8): 3936-3943.

Chen, X., Verma, R., Espinoza, D. N., et al. Pore-scale determination of gas relative permeability in hydrate-bearing sediments using X-ray computed micro-tomography and lattice Boltzmann method. Water Resources Research, 2018, 54(1): 600-608.

Clarke, M. A., Pooladi-Darvish, M., Bishnoi, P. R. A method to predict equilibrium conditions of gas hydrate formation in porous media. Industrial & Engineering Chemistry Research, 1999, 38(6): 2485-2490.

Cui, Y., Lu, C., Wu, M., et al. Review of exploration and production technology of natural gas hydrate. Advances in Geo-Energy Research, 2018, 2(1): 53-62.

Dai, S., Seol, Y. Water permeability in hydrate-bearing sediments: A pore-scale study. Geophysical Research Letters. 2014, 41(12): 4176-4184.

Dong, H., Blunt, M. J. Pore-network extraction from micro-computerized-tomography images. Physical Review E, 2009, 80(3): 036307.

Gong, B., Zhang, R., Sun, T., et al. Coupling model of submarine deformation response prediction during methane hydrate exploitation. Energy & Fuels, 2022, 36(13): 6785-6809.

He, J., Li, X., Chen, Z. Effective permeability changes during hydrate production. Energy, 2023, 282: 128887.

Jang, J., Santamarina, J. C. Recoverable gas from hydrate-bearing sediments: Pore network model simulation and macroscale analyses. Journal of Geophysical Research: Solid Earth, 2011, 116(B08): B08202.

Kleinberg, R. L., Flaum, C., Straley, C., et al. Seafloor nuclear magnetic resonance assay of methane hydrate in sediment and rock. Journal of Geophysical Research: Solid Earth, 2003, 108(B3): 2137.

Koh, C. A., Westacott, R. E., Zhang, W., et al. Mechanisms of gas hydrate formation and inhibition. Fluid Phase Equilibria, 2002, 194-197: 143-151.

Kvamme, B. Kinetics of hydrate formation, dissociation and reformation. Chemical Thermodynamics and Thermal Analysis, 2021, 1-2: 100004.

Lei, L., Santamarina, J. C. Laboratory strategies for hydrate formation in fine-grained sediments. Journal of Geophysical Research: Solid Earth, 2018, 123(4): 2583-2596.

Li, G., Zhan, L., Yun, T., et al. Pore-scale controls on the gas and water transport in hydrate-bearing sediments. Geophysical Research Letters, 2020, 47(12): e2020GL086990.

Liu, L., Zhang, Z., Li, C., et al. Hydrate growth in quartzitic sands and implication of pore fractal characteristics to hy-

draulic, mechanical, and electrical properties of hydrate-bearing sediments. Journal of Natural Gas Science and Engineering, 2020, 75: 103109.

Li, Y., Liu, L., Jin, Y., et al. Characterization and development of marine natural gas hydrate reservoirs in clayey-silt sediments: A review and discussion. Advances in Geo-Energy Research, 2021, 5(1): 75-86.

Li, Y., Xu, T., Xin, X., et al. Pore-scale study of the dynamic evolution of multi-phase seepage parameters during hydrate dissociation in clayey silt hydrate-bearing sediments. Journal of Hydrology, 2024, 635: 131178.

Lu, C., Qin, X., Sun, J., et al. Research progress and scientific challenges in the depressurization exploitation mechanism of clayey-silt natural gas hydrates in the northern South China Sea. Advances in Geo-Energy Research, 2023, 10(1): 14-20.

Luo, Y., Sun, Y., Li, L., et al. Image-based pore-network modeling of two-phase flow in hydrate-bearing porous media. Energy, 2022, 252: 124044.

Mahabadi, N., Dai, S., Seol, Y., et al. Impact of hydrate saturation on water permeability in hydrate-bearing sediments. Journal of Petroleum Science and Engineering, 2019, 174: 696-703.

Mahabadi, N., Dai, S., Seol, Y., et al. The water retention curve and relative permeability for gas production from hydrate-bearing sediments: Pore-network model simulation. Geochemistry, Geophysics, Geosystems, 2016a, 17(8): 3099-3110.

Mahabadi, N., Zheng, X., Jang, J. The effect of hydrate saturation on water retention curves in hydrate-bearing sediments: Water retention curves in THF HBS. Geophysical Research Letters, 2016b, 43(9): 4279-4287.

Ma, J., Sanchez, J. P., Wu, K., et al. A pore network model for simulating non-ideal gas flow in micro-and nano-porous materials. Fuel, 2014, 116: 498-508.

Pan, L., Lei, L., Seol, Y. Pore-scale influence of methane hydrate on permeability of porous media. Journal of Natural Gas Science and Engineering, 2021, 87: 103758.

Ruppel, C. D., Kessler, J. D. The interaction of climate change and methane hydrates: Climate-hydrates interactions. Reviews of Geophysics, 2017, 55(1): 126-168.

Seol, Y., Kneafsey, T. J. Methane hydrate induced permeability modification for multiphase flow in unsaturated porous media. Journal of Geophysical Research: Solid Earth, 2011, 116(B08): B08102.

Sloan Jr, E. D., Koh, C. A. Clathrate Hydrates of Natural Gases. Boca Raton, USA, CRC Press, 2007.

Sourav, K. S., Angus, I. B. The influence of gas hydrate morphology on reservoir permeability and geophysical shear wave remote sensing. Journal of Geophysical Research: Solid Earth, 2021, 126(11): e2021JB022206.

Sun, J., Dong, H., Arif, M., et al. Influence of pore structural properties on gas hydrate saturation and permeability: A coupled pore-scale modeling and X-ray computed tomography method. Journal of Natural Gas Science and Engineering, 2021, 88: 103805.

Wu, N., Zhang, H., Yang, S., et al. Gas hydrate system of Shenhu Area, Northern South China Sea: Geochemical results. Journal of Geological Research, 2011, 2011: 370298.

Wu, P., Li, Y., Sun, X., et al. Pore-scale 3D morphological modeling and physical characterization of hydrate-bearing sediment based on computed tomography. Journal of Geophysical Research: Solid Earth, 2020, 125(12): e2020JB020570.

Xia, Y., Elsworth, D., Cai, J., et al. Pore-scale water-gas distribution and gas permeability of natural gas hydrate reservoirs in the South China Sea. Geoscience Frontiers, 2024, 15(4): 101816.

Xia, Y., Xu, S., Lu, C., et al. Characterization and capillary pressure curve estimation of clayey-silt sediment in gas hydrate reservoirs of the South China Sea. Advances in Geo-Energy Research, 2023, 10(3): 200-207.

Xu, Z., Yoshihiro, K. Morphological change of hydrate caused by Ostwald ripening and sintering. Energy & Fuels, 2025, 39(9): 4238-4248.

Yang, Y., Cai, S., Yao, J., et al. Pore-scale simulation of remaining oil distribution in 3D porous media affected by wettability and capillarity based on volume of fluid method. International Journal of Multiphase Flow, 2021, 143: 103746.

Yan, R., Hayley, J., Priest, J. A. Modeling water retention curve of hydrate-bearing sediment. International Journal of Geomechanics, 2020, 20(2): 04019179.

You, K., Flemings, P. B., Malinverno, A., et al. Mechanisms of methane hydrate formation in geological systems. Reviews of Geophysics, 2019, 57(4): 1146-1196.

Yousif, M. H., Abass, H. H., Selim, M. S.,et al. Experimental and theoretical investigation of methane-gas-hydrate dissociation in porous media. SPE Reservoir Engineering, 1991, 6(1): 69-76.

Yu, Y., Zhang, X., Liu, J., et al. Natural gas hydrate resources and hydrate technologies: A review and analysis of the associated energy and global warming challenges. Energy & Environmental Science, 2021, 14(11): 5611-5668.

Zhang, Y., Li, C., Ma, J., et al. Investigating the effective permeability evolution as a function of hydrate saturation in the hydrate-bearing sands using a kinetic-theory-based pore network model. Computers and Geotechnics, 2022a, 150: 104930.

Zhang, Y., Liu, L., Wang, D., et al. Application of low-field nuclear magnetic resonance (LFNMR) in characterizing the dissociation of gas hydrate in a porous media. Energy & Fuels, 2021, 35(3): 2174-2182.

Zhang, Z., Wu, N., Liu, C., et al. Molecular simulation studies on natural gas hydrates nucleation and growth: A review. China Geology, 2022b, 5(2): 330-344.

Zhao, Z., Zhou, X. Pore-scale effect on the hydrate variation and flow behaviors in microstructures using X-ray CT imaging. Journal of Hydrology, 2020, 584: 124678.

Zheng, J., Chong, Z., Qureshi, M. F., et al. Carbon dioxide sequestration via gas hydrates: A potential pathway toward decarbonization. Energy & Fuels, 2020, 34(9): 10529-10546.